

# Study of the mechanical properties of Nd:YVO<sub>4</sub> crystal by use of laser interferometry and finite-element analysis

Xiaoyuan Peng, Anand Asundi, Yihong Chen, and Zhengjun Xiong

A hybrid method that combines experimental and numerical approaches for determining the material properties of Nd:YVO<sub>4</sub> is reported. In the experimental investigations a laser interferometer is proposed for measuring the physical deformation of lasing materials at the end-pump surface. By matching with the measured end bulging, we have implemented a numerical solution with finite-element analyses to determine the Poisson ratio and Young's modulus of the crystal. The accuracy interval of the evaluated Poisson ratio of 0.33 and Young's modulus of 133 GPa is discussed numerically. Based on the mechanical properties obtained, the end effect is separated from thermal effects, and it shows that the end effect results in an approximate equal thermal lensing effect compared with the index parts for end-pumped Nd:YVO<sub>4</sub> lasers. © 2001 Optical Society of America

OCIS codes: 140.3480, 140.6810, 120.3180, 160.3380.

## 1. Introduction

Diode-pumped solid-state lasers are compact, efficient, and stable and have diffraction-limited beam quality and high-power output.<sup>1-3</sup> Recently, a new lasing material, Nd:YVO<sub>4</sub>, applied to diode-pumped solid-state (DPSS) lasers is attracting more attention owing to its high efficiency.<sup>4,5</sup> Much research has been engaged in scaling the Nd:YVO<sub>4</sub> lasers to high average power through theoretical analyses and experimental investigations.<sup>6,7</sup> It is a common fact that the maximum incident pump power is limited by the stress fracture, which is caused by nonuniform temperature distributions in the crystals with pump loading. Because the stress fracture is determined by the inherent material properties of lasing crystals, i.e., the Poisson ratio and Young's modulus, they are important parameters for designing and analyzing DPSS lasers. For Nd:YAG it has been known that Young's modulus, the Poisson ratio, and the maximum hoop stress are 307 GPa, 0.3, and 20,000 psi, respectively.<sup>8</sup> However, the mechanical properties

of Nd:YVO<sub>4</sub> are still unknown. It is therefore difficult to calculate theoretically its stress distribution, end bulging, and thermally induced birefringence effect as well as to predict the maximum laser output power.

In diode-end-pumped solid-state lasers, inhomogeneous local heating of laser materials and nonuniform temperature distribution in lasing crystals result in distortion of the laser beam that is due to temperature- and stress-dependent variations of the refractive index and the end bulging of the pumped surface.<sup>8</sup> Both effects contribute to the formation of a thermal lens and are referred to as the index parts and the end effect, respectively.<sup>8,9</sup> Such aberrated thermal lenses induced by index parts and the end effect significantly limit laser-beam quality, resonator stability, and output laser power.<sup>10-12</sup> Koehler<sup>8</sup> evaluated the end effect for a side-pumped Nd:YAG system to be less than 6% in the thermal effects. Recently, Weber *et al.*<sup>13</sup> calculated the end effect numerically with a two-dimensional finite-element (FE) analysis and concluded that the average thermal lens induced by the end effect had a proportion of ~30% for the end-pumped edge-cooled Nd:YAG system. Baer *et al.*<sup>9</sup> Kleine *et al.*,<sup>10</sup> and Marshall *et al.*<sup>12</sup> directly measured the distortion of the end-pump surface and index parts by use of interferometric techniques. They showed that the thermal lensing effect and aberrations for Nd:YLF and Nd:YVO<sub>4</sub> are strong at the pump facet for end-pumped solid-state lasers with several watts of output. In addition, index parts and the end effect make approximately

X. Peng (p144867779@ntu.edu.sg) and A. Asundi are with the Photonics Program, Nanyang Technological University, Nanyang Avenue, Singapore 639798, Singapore. Y. Chen and Z. Xiong are with the Gintec Institute of Manufacturing Technology, 71 Nanyang Drive, Singapore 638075, Singapore.

Received 24 May 2000; revised manuscript received 23 October 2000.

0003-6935/01/091396-08\$15.00/0

© 2001 Optical Society of America

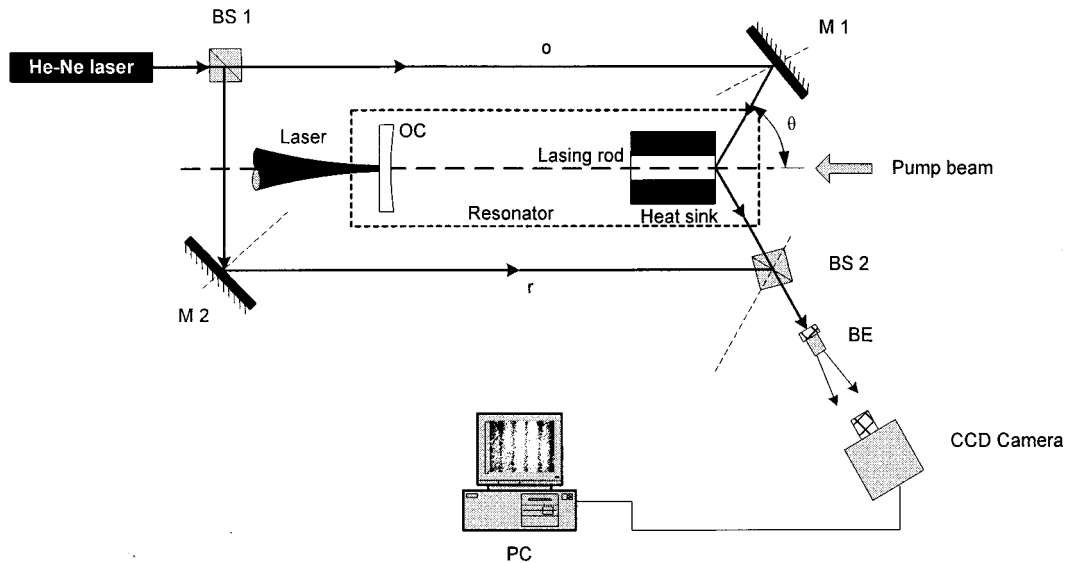


Fig. 1. Schematic layout of the DPSS laser system and the experimental setup of the laser interferometer.

equal contributions to aberrations. Inasmuch as the end effect is in fact a kind of mechanical displacement at the end-pump surface, end bulging provides an essential parameter for studying the properties and behaviors of lasing crystals. The accurate experimental results of thermally induced end bulging enable the subsequent determination of strain and stress. More important, these results serve as exact measured data for comparison with computational simulations when a FE method is used for the analysis of material properties.

Here we use a hybrid method that combines experimental and numerical approaches to determine the material properties of the Nd:YVO<sub>4</sub> crystal. With respect to experimental investigations, a laser interferometer is proposed to measure the end effect of lasing crystals. The proposed optical interferometric technique provides a noninvasive, high-resolution means of diagnosing the end effect by measuring variations of the optical path difference (OPD) induced by thermal loading on lasing crystals without disturbing the normal working condition of DPSS lasers. With the numerical approach, by matching the measured end bulging, the FE model involves strain–stress calculations to fit the Poisson ratio and Young’s modulus. In addition, the numerical solution allows discussions of the accuracy interval of the evaluated mechanical properties. With the values obtained, the end effect can be separated theoretically from the thermal effects for end-pumped Nd:YVO<sub>4</sub> lasers.

## 2. Laser System and Interferometry

Figure 1 shows a schematic layout of the diode-end-pumped edge-cooled Nd:YVO<sub>4</sub> laser system and the experimental setup of the interferometer used to quantify the end effect. A 3 mm × 3 mm × 5 mm Nd:YVO<sub>4</sub> crystal with a Nd<sup>3+</sup> doping concentration of 0.5 at. % was the active lasing medium. The crystal

had a 1.06- $\mu\text{m}$  antireflection coating at one end surface and a 1.06- $\mu\text{m}$  high-reflection coating and an 808-nm antireflection coating at the pump-end surface. Wrapped in an indium foil layer with high thermal conductivity, the crystal was mounted on a copper heat sink. The heat deposited in the crystal was radially removed by the heat sink, whose periphery was cooled by water with a temperature of 23 °C. Two end surfaces of the crystal were in contact with air. The crystal was end pumped by a fiber-coupled diode laser with a central wavelength of 808 nm, and its output power ranged from 0 to 15 W. The pump beam from the fiber optics with a numerical aperture of 0.16 and a diameter of 1.5 mm was focused to a spot of 0.2-mm radius by collimating and focusing optics. The laser resonator consisted of a high-reflection-coated end surface of Nd:YVO<sub>4</sub> and an output coupler, OC, with a curvature radius of 400 mm and a transmission of 11%. The length of the cavity could be adjusted from 100 to 300 mm, which resulted in a beam-waist diameter from 300 to 600  $\mu\text{m}$  at the flat mirror. The input–output characteristics of the diode-end-pumped edge-cooled TEM<sub>00</sub> Nd:YVO<sub>4</sub> laser system is shown in Fig. 2. The TEM<sub>00</sub> optical-to-optical efficiency and slope efficiency for this laser system at 5-W output levels were approximately 42% and 51%, respectively.

With regard to the laser interferometer a frequency-stabilized He–Ne laser with a wavelength of 0.6328  $\mu\text{m}$  was employed as the light source. The laser beam was split into two paths as the reference beam, *r*, and object beam, *o*, by a beam splitter, BS 1. Two flat mirrors, M 1 and M 2, were at a working wavelength. The object beam was guided to reflect on the crystal surface at an angle of 66°. Therefore the interference patterns involved information from the pump surface. Another beam splitter cube, BS 2, was used to combine the two beam paths, and the beam expander, BE, was used to magnify the inter-

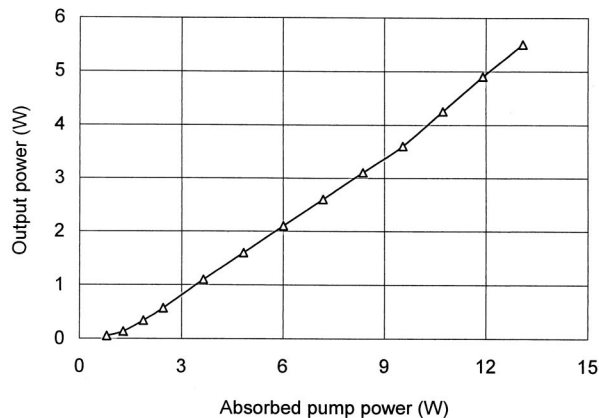


Fig. 2. Input–output characteristics of the diode-end-pumped edge-cooled Nd:YVO<sub>4</sub> laser.

ferograms. The generated interference patterns were taken by a CCD camera connected to a PC and a digital video recording system. The video system had a temporal resolution of 1/30 s. Because no additional optical element was inserted into the laser resonator, the actual lasing operation was not disturbed by such a laser–interferometer arrangement. Figures 3(a), 3(b), and 3(c) show the fringe patterns that are typically taken from absorbed pump powers of 0, 5, and 10 W, respectively.

The end-bulging vector  $\mathbf{d}_e(P)$  at point P on the surface in the direction of the sensitivity vector  $\mathbf{e}(P)$  is related to the phase difference  $\Delta\phi(P)$ :

$$\Delta\phi(P) = \frac{2\pi}{\lambda} \mathbf{d}_e(P) \cdot \mathbf{e}(P). \quad (1)$$

The phase difference caused by end bulging is

$$\Delta\phi(P) = \frac{2\pi}{\lambda} \text{OPD}, \quad (2)$$

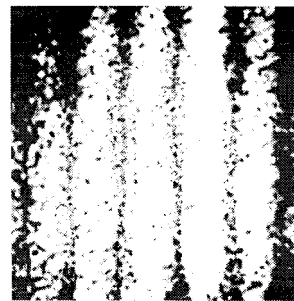
where  $\lambda$  is the wavelength of the probe beam. The end bulging together with the sensitivity vector gives OPD's that lead to observable fringe patterns. In such an interferometric setup the sensitivity vector coincides with the direction of the bulging component, enabling the measurement to be performed with the highest sensitivity.<sup>14</sup> From Eq. (1) the end bulging is given by

$$d_e(P) = \frac{\lambda \Delta\phi(P)}{4\pi \cos(\theta)}, \quad (3)$$

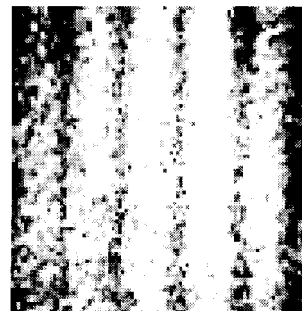
where  $d_e(P)$  is the end bulging at point P,  $\theta$  is the angle between the longitudinal direction and the illumination direction, and  $\Delta\phi(P)$  is the interference phase variation at point P.

Based on Eq. (3), the end bulging as a function of absorbed pump power can be calculated, as shown in Fig. 4. The solid line in Fig. 4 represents the measured result from FE simulation, which is explained in Section 3.

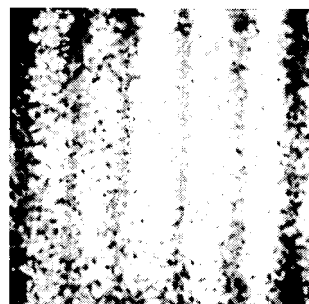
It is explicit that the end bulging of Nd:YVO<sub>4</sub> crys-



(a)



(b)



(c)

Fig. 3. Interferograms of the end effect for an end-pumped Nd:YVO<sub>4</sub> laser at absorbed pump powers of (a) 0 W, (b) 5 W, and (c) 10 W.

tal becomes more serious with an increase of absorbed pump power. The maximum end bulging of 1.97  $\mu\text{m}$  occurs at the absorbed pump power of 10 W. As part of the thermal effects, the end bulging causes aberrations in the laser beam. In addition, it causes the crystal to fracture when induced stress inside the crystal exceeds the ultimate stress. The measured end bulging, then, can offer comparison data in FE analysis to evaluate the unknown mechanical properties of Nd:YVO<sub>4</sub>.

### 3. Numerical Model and Results

#### A. Theory

The three-dimensional (3-D) FE model shown in Fig. 5 was developed for one-fourth of the cuboid brick and represents the entire operation characteristic of the crystal. The three kinds of material considered for this model were Nd:YVO<sub>4</sub> crystal, the copper heat

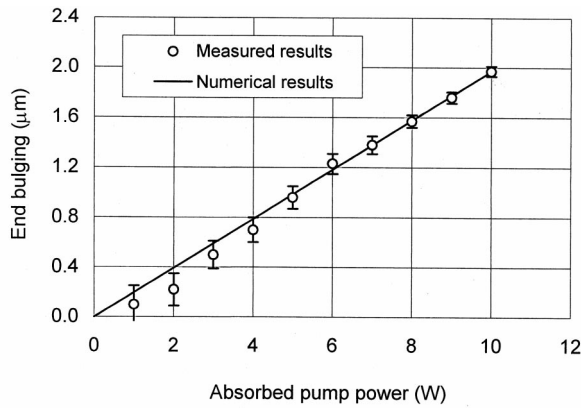


Fig. 4. End bulging as a function of absorbed pump power obtained by numerical and experimental approaches.

sink, and indium foil, with their thermodynamic parameters as listed in Table 1.

The temperature distribution  $T(x, y, z)$  is described by a 3-D heat conduction equation<sup>13</sup>:

$$\nabla^2 T(x, y, z) + \frac{q(x, y, z)}{k} = 0, \quad (4)$$

where  $q(x, y, z)$  is the heat source that is part of the pump power and  $k$  is the thermal conductivity.

The heat flow through the surface of the crystal

defines the boundary conditions. Based on Newton's law of heat transfer, it is

$$K \frac{\partial T}{\partial n} \Big|_s = h(T_c - T|_s), \quad (5)$$

where  $T_c$  is the cooling or air temperature, which is taken as a constant,  $T|_s$  is the local temperature of the crystal surface,  $n$  is the local normal to that surface, and  $h$  is the heat transfer coefficient. The heat transfer coefficient of indium in contact with Nd:YVO<sub>4</sub> and indium in contact with copper is assumed to be  $1.5 \times 10^{-2} \text{ W K}^{-1} \text{ mm}^{-2}$ . Two air-contacted endfaces have a heat transfer coefficient of  $6.5 \times 10^{-6} \text{ W K}^{-1} \text{ mm}^{-2}$ .

The steady heat source, which is described as a Gaussian distribution, applies heat generation rates to the crystal (heat flow rate per unit volume) as<sup>13</sup>

$$q(x, y, z) = \eta_{\text{heat}} P_0 p(x, y, z) \frac{\alpha_T}{1 - \exp(-\alpha_T L)} \exp(-\alpha_T z), \quad (6)$$

$$p(x, y, z) = \frac{1}{\pi \omega_p^2} \exp\left[-\frac{2(x^2 + y^2)}{\omega_p^2}\right], \quad (7)$$

$$\omega_p^2 = \omega_0^2 \left\{ 1 + \left[ \frac{\lambda_p(z - z_0)}{\pi n_0 \omega_0^2} \right]^2 \right\}, \quad (8)$$

where  $p(x, y, z)$  is the normalized pump radiation distribution,  $P_0$  is the total incident pump power,  $L$  is the doped length of the rod,  $\alpha_T$  is the absorption

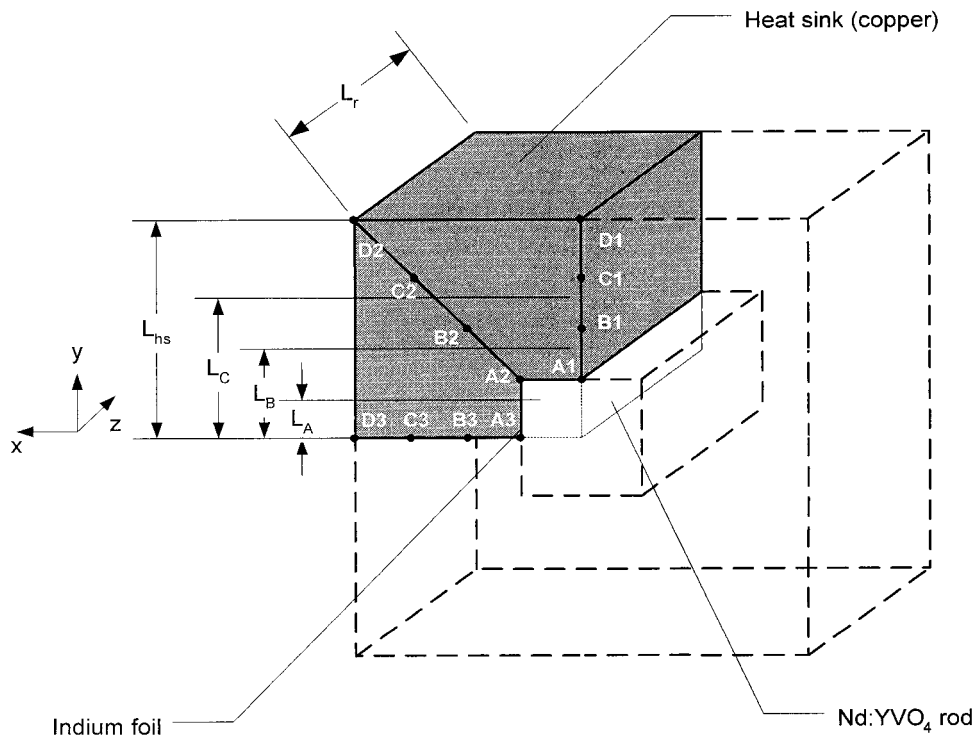


Fig. 5. Three-dimensional FE model of the Nd:YVO<sub>4</sub> brick including the copper heat sink and indium foil.

Table 1. Thermodynamic Parameters of Nd:YVO<sub>4</sub>, Copper, and Indium Foil

Parameters	Nd:YVO <sub>4</sub>	Copper	Indium foil
Thermal conductivity (W m <sup>-1</sup> K <sup>-1</sup> )	5.23 (  c) 5.10(⊥c)	111	5.1
Thermal expansion coefficient (1 × 10 <sup>-6</sup> K <sup>-1</sup> )	11.37 (  c) 4.43(⊥c)	—	3.412
Heat capacity (kJ kg <sup>-1</sup> K <sup>-1</sup> )	0.8	0.38	0.2
Density (1 × 10 <sup>-3</sup> kg/cm <sup>3</sup> )	4.24	8.6	1.1

coefficient,  $\omega_p$  is the radius of the pump beam,  $\omega_0$  is the waist radius of the pump beam at the position of  $z_0$ ,  $\lambda_p$  is the wavelength of the pump beam,  $n_o$  is the refractive index of the crystal, and  $\eta_{\text{heat}}$  represents the fraction of pump power converted to heat. According to Ref. 15,  $\eta_{\text{heat}}$  is 0.24 for a 0.5-at. % doped Nd:YVO<sub>4</sub> crystal in lasing conditions.

### B. Finite-Element Model

Three-dimensional thermal conduction based on Eq. (4) is considered for the calculation of temperature distributions in anisotropic laser crystal, taking into account the anisotropy in the thermal conductivity of Nd:YVO<sub>4</sub> crystal. The presence of thermal conductivity along the sagittal and the longitudinal directions is different. However, since the anisotropic 3-D thermal conduction equations are difficult to solve by analytical methods, we treat the complex 3-D thermal conduction with FE numerical implementation. The crystal is divided into a number of infinitesimal elements. The terms  $x, y, z$  are the variables of the tangential, the sagittal, and the longitudinal coordinates. They represent discrete longitudinal elements,  $z = 1-30$ , covering the crystal length  $L$  (5 mm) as well as discrete transverse elements  $x$  and  $y$  from 1 to 15, covering the cross dimension of the crystal (1.5 mm). The indium foil with a thickness of 0.2 mm is divided into two layers, and the copper wrap around the crystal is transversely meshed into six layers. The marked points in Fig. 5 are selected to testify to the validity of the FE model when their corresponding temperatures are compared between calculated and experimental results, where  $L_{hs}$ ,  $L_C$ ,  $L_B$ , and  $L_A$  are set at 5, 3.7, 2.6, and 1.5 mm, respectively. Here, temperature constraints of 23° and 26 °C are applied to the periphery of the heat sink and air, respectively, as boundary conditions and the insulation process on the symmetrical section. The numerical implementation is based on Eqs. (4)–(8) with ANSYS 5.4.<sup>16</sup> The accuracy of the FE analysis depends on the numerical solution of the algorithm and the values of the input parameters, such as ma-

terial thermodynamic properties and boundary conditions. To realize high-accuracy calculations, the FE model is examined by experiment.

When the numerical and the experimental results in Table 2, are compared the deviations between the calculated and the measured temperature at the corresponding points are less than 2%. Consequently, the FE model is validated for high accuracy for numerical simulations. Figure 6 demonstrates the sagittal and the longitudinal temperature profiles in the Nd:YVO<sub>4</sub> crystal at the absorbed pump power of 10 W. The temperature distributions along the  $x$  and  $y$  axes are almost the same owing to the slight difference in the thermal conductivity between these two directions. In addition, the longitudinal temperature gradient is much larger near the pump region where the strongest absorption occurs.

### C. Structure Analysis

Based on the temperature distributions obtained, the stress and strain are investigated by FE analyses. The equations of equilibrium of stresses in the Cartesian coordinates are given by<sup>17</sup>

$$\frac{\partial \sigma_{xx}}{\partial x} + \frac{\partial \sigma_{xy}}{\partial y} + \frac{\partial \sigma_{xz}}{\partial z} = 0, \tag{9}$$

$$\frac{\partial \sigma_{yx}}{\partial x} + \frac{\partial \sigma_{yy}}{\partial y} + \frac{\partial \sigma_{yz}}{\partial z} = 0, \tag{10}$$

$$\frac{\partial \sigma_{xz}}{\partial x} + \frac{\partial \sigma_{yz}}{\partial y} + \frac{\partial \sigma_{zz}}{\partial z} = 0, \tag{11}$$

where the stress components  $\sigma_{ii}$  represent normal components and  $\sigma_{ij}$ , where  $i$  is not equal to  $j$ , represents shear components where the subscript  $i$  or  $j$  represents  $x, y$ , or  $z$ . In Eqs. (9)–(11) it is assumed that the shear stresses are symmetric to exclude the case of the turning moment on the crystal. This statement is expressed as  $\sigma_{ij} = \sigma_{ji}$ , where  $i$  here is not equal to  $j$ .

Table 2. Measured and Calculated Temperature Values for an End-Pumped Nd:YVO<sub>4</sub> Laser

Temperature	Position											
	A1	B1	C1	D1	A2	B2	C2	D2	A3	B3	C3	D3
Measured	27	25	24	23	26	25	24	23	27	25	24	23
FE model	27.32	24.72	24.01	23.02	26.36	24.51	23.55	23.02	27.32	24.72	24.01	23.02

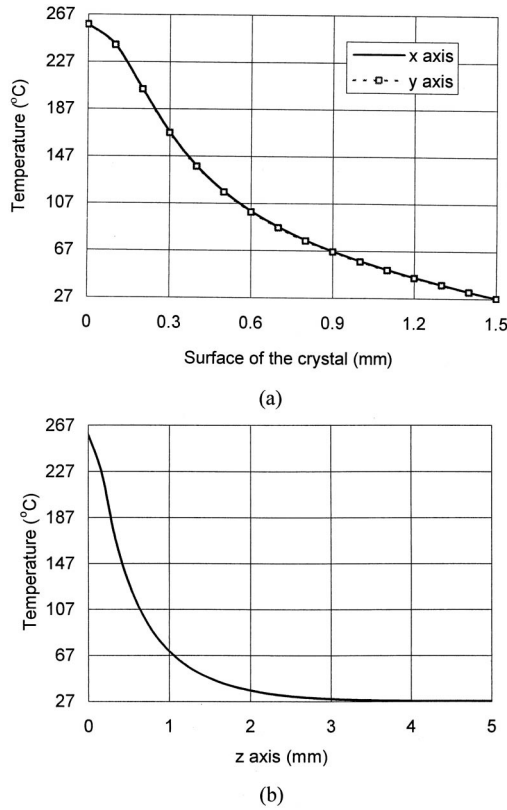


Fig. 6. Temperature profiles for the Nd:YVO<sub>4</sub> crystal at the pump surface and longitudinal direction: (a) sagittal temperature distributions at the pump surface along two directions of the  $x$  and  $y$  axes; (b) longitudinal temperature distributions along the  $z$  axis.

The strain–displacement relationships are defined as follows<sup>18</sup>:

$$\varepsilon_{ij} = \frac{1}{2} \left( \frac{\partial u_i}{\partial x_j} + \frac{\partial u_j}{\partial x_i} \right), \quad (12)$$

where  $\varepsilon_{ii}$  are direct strains in the  $x$ ,  $y$ , and  $z$  directions,  $\varepsilon_{ij}$  with  $i$  not equal to  $j$  represents shear strains,  $u_i$  represents displacements in the  $x$ ,  $y$ , and  $z$  directions.

According to Hooke's law, the following equations exist<sup>18</sup>:

$$\begin{aligned} \sigma_{xx} &= 2\mu\varepsilon_{xx} + \delta_{xx}[\xi e - (3\xi + 2\mu)\alpha_a T(x, y, z)], \\ \sigma_{yy} &= 2\mu\varepsilon_{yy} + \delta_{yy}[\xi e - (3\xi + 2\mu)\alpha_c T(x, y, z)], \\ \sigma_{zz} &= 2\mu\varepsilon_{zz} + \delta_{zz}[\xi e - (3\xi + 2\mu)\alpha_a T(x, y, z)], \\ \sigma_{xy} &= 2\mu\varepsilon_{xy}, \\ \sigma_{yz} &= 2\mu\varepsilon_{yz}, \\ \sigma_{xz} &= 2\mu\varepsilon_{xz}, \end{aligned} \quad (13)$$

where  $\delta_{ij}$  is the Kronecker delta function,  $T(x, y, z)$  is the temperature distribution inside the crystal,  $e$  is the sum of normal strains ( $e = \sum \varepsilon_{ii}$ ),  $\alpha$  is the thermal expansion coefficient,  $\xi$  and  $\mu$  are constants related to

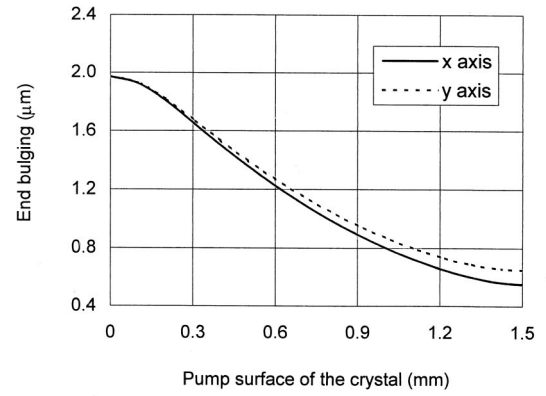


Fig. 7. Calculated end bulging of the crystal in the  $x$  and  $y$  axes at absorbed pump power of 10 W.

Young's modulus  $E$  and Poisson ratio  $\nu$ , which are given by

$$\xi = \frac{\nu E}{(1 + \nu)(1 - 2\nu)}, \quad (14)$$

$$\mu = \frac{E}{2(1 + \nu)}. \quad (15)$$

According to Eqs. (9)–(15), the stresses and strains in the crystal under prescribed temperature distributions can be simulated by the FE model. Note that the mechanical properties of the Nd:YVO<sub>4</sub> crystal are assumed to be isotropic in our calculations. With respect to the boundary condition of the structure model the crystal normal displacement on the mounted periphery is set at zero. When matched with the measured end bulging, the Poisson ratio and Young's modulus can be determined by numerically implementing the FE model. For example, consider the FE model in the case of absorbed pump power of 10 W and corresponding maximum end bulging of 1.97  $\mu\text{m}$  shown in Fig. 4. In our numerical simulations the Poisson ratio and Young's modulus are fitted to be 133 GPa and 0.33, respectively, with which the calculated end bulging of the crystal in the  $x$  and  $y$  axes is shown in Fig. 7. The maximum end bulging is equal to the measured value of 1.97  $\mu\text{m}$  at the absorbed pump power of 10 W. Note that the end bulging in the  $y$  axis is larger than that in the  $x$  axis because the thermal expansion coefficients in the  $x$  axis of  $4.43 \times 10^{-6} \text{ K}^{-1}$  and the  $y$  axis of  $11.37 \times 10^{-6} \text{ K}^{-1}$  are much different. In fact, the temperature gradient in the  $x$  axis is slightly higher than that in the  $y$  axis, which in turn results in slightly greater end bulging in the  $x$  axis. However, the thermal expansion coefficient in the  $y$  axis is almost three times larger than that in the  $x$  axis. The calculation therefore shows that end bulging in the  $y$  axis is larger than that in the  $x$  axis.

#### D. Discussion

Since the numerical model allows accuracy discussions on evaluated mechanical properties, we can cal-

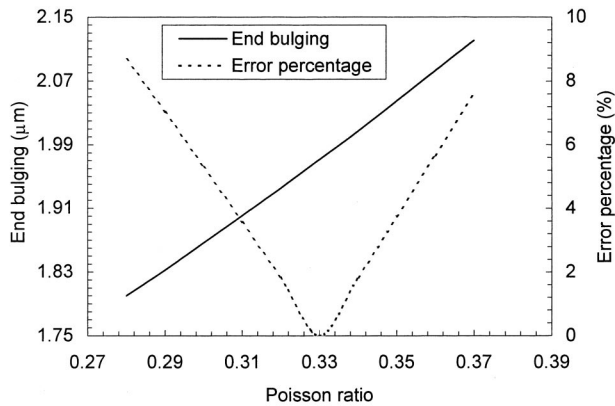


Fig. 8. Calculated end bulging as a function of the Poisson ratio ( $E = 133$  GPa).

culate the accuracy interval of the Poisson ratio and Young's modulus. When we vary the Poisson ratio by using the numerical model from 0.28 to 0.37 with a spacing of 0.1 while the Young's modulus stays at 133 GPa, we can show in Fig. 8 a variation of maximum end bulging as a function of the Poisson ratio. It can be found that the error percentage becomes larger with the increasing deviation of the Poisson ratio from 0.33. Because the measurement accuracy of the laser interferometry is considered within the range of 5%,<sup>19</sup> the accuracy interval of the Poisson ratio is therefore determined to be from 0.315 to 0.345. Furthermore, we can compare the calculated and measured end bulging as a function of absorbed pump power, the results of which are shown in Fig. 4. It can be found that the numerical results are in good agreement with the measured end bulging when the absorbed pump power is greater than 5 W, because a greater end bulging contributes to higher measurement accuracy.

In addition, the evaluated Young's modulus can be testified by the calculation of thermal shock parameter  $R$ , which indicates permissible thermal loading before the fracture occurs. The thermal shock parameter depends on the mechanical and the thermal properties of the host material and is given by

$$R = \frac{K\sigma_{\max}}{\alpha E}, \quad (16)$$

where  $\sigma_{\max}$  is the maximum tensile stress.

In our experiment a fracture that runs from the crystal center to the circumference and perpendicular to the  $y$  axis is observed to occur in 1-at. % Nd<sup>3+</sup>-doped Nd:YVO<sub>4</sub> with an absorbed pump power of 22 W and a pump beam radius of 0.2 mm with identical cooling geometry. Based on Ref. 20, the fractional thermal loading for 1-at. % Nd<sup>3+</sup>-doped Nd:YVO<sub>4</sub> crystal is 0.36. By implementing the numerical model by use of evaluated mechanical parameters, we determined the fracture tensile stress to be 53 MPa. From Eq. (16) the thermal shock parameter is then calculated to be 4.77 W/cm, which is in agreement with the measured value of 4.8 W/cm obtained

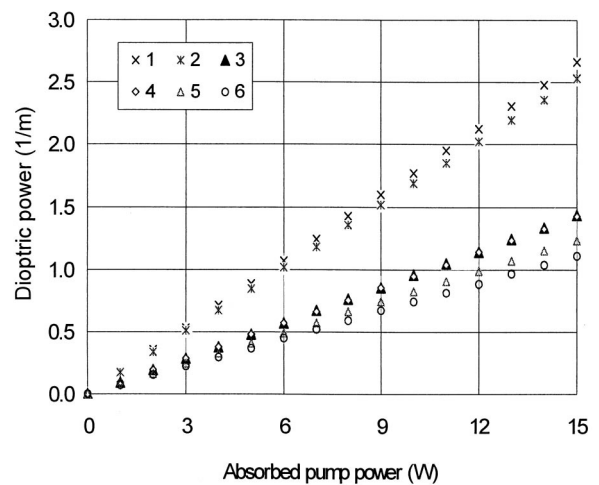


Fig. 9. Calculated dioptric power as a function of absorbed pump power; 1 and 2, 3 and 4, 5 and 6 are total dioptric power, the index part, and the end effect along the  $x$  and  $y$  axes, respectively.

by Chen.<sup>6</sup> When the Poisson ratio maintains a constant of 0.33, an accuracy interval of the evaluated Young's modulus of 133 GPa can be examined in a range of 10%. Based on the determined mechanical properties, the thermal lensing effect induced by the end effect as a function of the absorbed pump power can be calculated for end-pumped edge-cooled Nd:YVO<sub>4</sub> lasers. Referring to Ref. 13, we see that the thermally induced spherical lens allows an approximate estimate of the OPD. When aberrations are neglected, the OPD( $r$ ) induced by a spherical lens depends quadratically on the pump beam radius  $r$ . The dioptric power  $D$  of the thermal lens is

$$D = \frac{2[\text{OPD}(r) - \text{OPD}_0]}{r^2}, \quad (17)$$

where  $\text{OPD}_0$  is the optical path difference of the optical axis and  $r$  is the distance from the optical axis.

The dioptric power induced by the end effect is shown in Fig. 9. For comparison, Fig. 9 includes the thermal lensing effects induced by index parts and the total dioptric power. It can be seen that dioptric power presents a trend in linear increase with the rise in absorbed pump power. The end effect takes a proportion of 46% and 44% along the  $x$  and the  $y$  axes, respectively. The slight difference in the thermal lens between these two directions is due to the anisotropic property of the Nd:YVO<sub>4</sub> crystals; e.g., the thermal expansion coefficient, the thermal optical coefficient, and the thermal conductivity differ along the  $x$  and  $y$  axes. The numerical calculations show the conclusion that the end effect is approximately equal to the index parts in end-pumped Nd:YVO<sub>4</sub> laser systems, which coincides with the experimental results of Baer *et al.*<sup>9</sup>

#### 4. Conclusions

The material properties of lasing crystals, i.e., the Poisson ratio and Young's modulus, are important

parameters for the designing and analysis of DPSS lasers. A hybrid method that combines experimental and numerical approaches has been employed to determine the material properties of Nd:YVO<sub>4</sub>. The advantage of combining laser interferometry and a numerical analysis is visualization of the stress-strain state inside the crystal with the measured displacement only. We used a laser interferometer to measure the end bulging of Nd:YVO<sub>4</sub> at the end pump face in lasing conditions. We obtained the maximum end bulging that is due to thermal expansion of the laser crystal as a function of the absorbed pump power. The end effect measured here shows a maximum end bulging of 1.97 μm with absorbed pump power of 10 W. By comparing the measured end effect with the end bulging, we were able to use the numerical solution with the FE analyses to evaluate the material properties. With the valid FE model together with the measured end bulging, the Poisson ratio and Young's modulus were fitted at 0.33 and 133 GPa, respectively. The numerical model allows accuracy discussions on the mechanical parameters obtained. When measurement error was considered, the accuracy interval of the Poisson ratio was from 0.315 to 0.345 and Young's modulus was in the range of 10%. Finally, the parameters were evaluated to separate the end effect from thermal effects numerically. The calculated results show that the end effect is approximately equal to the index parts in Nd:YVO<sub>4</sub> laser systems.

This research was supported by the National Science and Technology Board and Nanyang Technological University through grants I99-P0-129 and MLC1/97, respectively. The authors are pleased to acknowledge the valuable help of G. Seet.

## References

1. T. Y. Fan and R. L. Byer, "Diode laser pumped solid-state lasers," *IEEE J. Quantum Electron.* **24**, 895–912 (1988).
2. S. C. Tidwell, J. F. Seamans, C. E. Hamilton, C. H. Muller, and D. D. Lowenthal, "Efficient, 15-W output power, diode-end-pumped Nd:YAG laser," *Opt. Lett.* **16**, 584–586 (1991).
3. D. Golla, M. Bode, S. Knoke, W. Schone, G. Ernst, and A. Tunnermann, "62-W CW TEM<sub>00</sub> Nd:YAG laser side-pumped by fiber-coupled diode lasers," *Opt. Lett.* **21**, 201–212 (1996).
4. W. L. Nighan, D. Dudley, and M. S. Keirstead, "Diode-bar-pumped Nd:YVO<sub>4</sub> lasers with >13-W TEM<sub>00</sub> output at >50% efficiency," in *Conference on Lasers and Electro-Optics*, Vol. 15 of 1995 OSA Technical Digest Series (Optical Society of America, Washington, D.C., 1995), pp. 17–18.
5. J. Zhang, M. Quade, K. M. Du, Y. Liao, S. Falter, M. Baumann, P. Loosen, and R. Poprawe, "Efficient TEM<sub>00</sub> operation of Nd:YVO<sub>4</sub> laser end pumped by fiber-coupled diode laser," *Electron. Lett.* **33**, 775–777 (1997).
6. Y. F. Chen, "Design criteria for concentration optimization in scaling diode end-pumped lasers to high powers: influence of thermal fracture," *IEEE J. Quantum Electron.* **35**, 234–239 (1999).
7. M. Tsunekane, N. Taguchi, T. Kaamatsu, and H. Inaba, "Analytical and experimental studies on the characteristics of composite solid-state laser rods in diode-end-pumped geometry," *IEEE J. Sel. Top. Quantum Electron.* **3**, 9–19 (1997).
8. W. Koechner, *Solid-State Laser Engineering*, 3rd ed. (Springer-Verlag, New York, 1992), pp. 388–392.
9. T. M. Baer, W. L. Nighan, and M. S. Keirstead, "Modeling of end-pumped, solid-state lasers," in *Conference in Lasers and Electro-Optics*, Vol. 11 of 1993 OSA Technical Digest Series (Optical Society of America, Washington, D.C., 1993), p. 638.
10. K. R. F. Kleine, L. P. Gonzalez, R. Bhatia, L. R. Marshall, and D. G. Matthews, "High brightness Nd:YVO<sub>4</sub> laser for nonlinear optics," *Advanced Solid-State Lasers*, M. M. Fejer, H. Injeyan, and U. Keller, eds., Vol. 26 of OSA Trends in Optics and Photonics Series (Optical Society of America, Washington, D.C., 1999), pp. 157–158.
11. T. S. Rose, B. Nighan, D. Dudley, R. A. Fields, D. Gilmore, and E. Hall, "Thermal lens reduction in longitudinally pumped diffusion bonded Nd:YVO<sub>4</sub>," in *Conference on Lasers and Electro-Optics*, Vol. 11 of 1997 OSA Technical Digest Series (Optical Society of America, Washington, D.C., 1997), p. 285.
12. L. R. Marshall, L. Gonzalez, R. Bhatia, K. Kleine, and D. G. Matthews, "Diode pumped lasers for the visible and ultraviolet," in *SOQUE Proceedings of Lasers '98, Tucson, Ariz.* (Society of Optics and Quantum Electronics, McLean, Va., 1998).
13. R. Weber, B. Neuenschwander, M. Macdonald, M. B. Roos, and H. P. Weber, "Cooling schemes for longitudinally diode laser-pumped Nd:YAG rods," *IEEE J. Quantum Electron.* **34**, 1046–1053 (1998).
14. T. Kreis, *Holographic Interferometry Principles and Methods* (Akademie Verlag, Berlin, 1996), pp. 78–82.
15. Y. F. Chen, T. M. Huang, C. F. Kao, C. L. Wang, and S. C. Wang, "Optimization in scaling fiber-coupled laser-diode end-pumped lasers to higher power: influence of thermal effect," *IEEE J. Quantum Electron.* **33**, 1424–1429 (1997).
16. P. C. Kohnke, *ANSYS: Engineering Analysis System Theoretical Manual* (Swanson Analysis Systems, Houston, Pa., 1986).
17. S. S. Rao, *The Finite Element Method in Engineering* (Butterworth-Heinemann, Boston, 1999).
18. B. A. Boley and J. H. Weiner, *Theory of Thermal Stresses* (Wiley, New York, 1960).
19. R. S. Sirohi and F. S. Chau, *Optical Methods of Measurement: Wholefield Techniques* (Marcel Dekker, New York, 1999).
20. J. L. Blows, T. Omatsu, J. Dawes, H. Pask, and M. Tateda, "Heat generation in Nd:YVO<sub>4</sub> with and without laser action," *IEEE Photonics Technol. Lett.* **10**, 1727–1729 (1998).